

# Fault Detection on Seismic Structural Images Using a Nested Residual U-Net

Kai Gao<sup>ID</sup>, Lianjie Huang<sup>ID</sup>, and Yingcai Zheng

**Abstract**—Automatic identification of faults on seismic structural images is a challenging yet crucial task in quantitative seismic interpretation. Human picking or attribute-based fault detection methods may misidentify faults on noisy, complex seismic images. We develop a new automatic fault detection method using a nested residual U-shaped convolutional neural network. Each of the encoders and decoders in this neural network is a residual U-Net, leading to a nested architecture. The final fault map results from the fusion of three fault maps with low, medium, and high fault resolutions. We demonstrate the excellent fault-detection capability of our nested neural network using a series of synthetic and field seismic images. We find that our approach produces clearer and more interpretable fault maps than the current state-of-the-art U-Net fault detection method, particularly on noisy seismic images. Our new automatic fault detection method can facilitate reliable quantitative seismic interpretation on field seismic images.

**Index Terms**—Convolutional neural network (CNN), deep learning, fault detection, nested residual U-Net (NRU), NRU-Net, seismic image, supervised machine learning, U-Net.

## I. INTRODUCTION

AUTOMATIC seismic interpretation extracts geologically meaningful information from subsurface seismic structural images or medium parameter models using computational, quantitative approaches [1]. Fault detection is one of the most important tasks in automatic seismic interpretation. Geologically, faults result from subsurface stress-induced rock formation brittle failure [2]. On seismic migration images, faults usually appear as lateral discontinuities of reflectors. Accurate imaging and subsequent identification of faults on seismic structural images provide crucial information in many applications, such as fluid injection and extraction in geothermal fields [3], [4], the caprock integrity in geologic carbon storage [5], and the extent, connectivity, and integrity of oil and gas reservoirs [6].

Yet, accurate and efficient identification of faults on field seismic images, particularly on noisy images with complex structures, could be challenging. Hand-picking of faults

Manuscript received December 16, 2020; revised March 3, 2021; accepted April 13, 2021. Date of publication April 29, 2021; date of current version December 23, 2021. This work was supported by the U.S. Department of Energy (DOE) Geothermal Technologies Office through the Los Alamos National Laboratory (LANL) under Contract 89233218CNA000001. (*Corresponding author: Kai Gao*)

Kai Gao and Lianjie Huang are with the Geophysics Group, Los Alamos National Laboratory, Los Alamos, NM 87545 USA (e-mail: kaigao@lanl.gov; ljh@lanl.gov).

Yingcai Zheng is with the Department of Earth and Atmospheric Sciences, University of Houston, Houston, TX 77204 USA.

Digital Object Identifier 10.1109/TGRS.2021.3073840

becomes infeasible when the target fault system is complex or contains numerous small-scale faults, especially on 3-D images. Semi-human-interfered approaches based on computing and analyzing seismic image attributes, such as semblance [7] and coherence [8]–[10], become problematic when undesired noises have a wavenumber spectrum similar to that of the image itself. Although studies attempted to improve attribute-based fault identification using, such as smoothing or constraining along or perpendicular to the fault features [10]–[12], these approaches usually require fine-tuning of one or many parameters based on characteristics of different images or the target faults. Some of these attribute-based methods also require a nontrivial computational cost, especially for large-scale 3-D image volumes.

Automatic seismic interpretation is emerging with the revitalization era of machine learning. Fault detection is particularly suitable for machine learning to carry out. Intuitively, a fault on a seismic image can be considered as a “yes” pixel compared with nonfault pixels (“no” pixels). Therefore, several studies used a classification neural network to detect faults on seismic images [13]–[15]. Alternatively, fault identification is analogous to image segmentation—finding faults on a seismic image based on lateral discontinuities of reflectors is similar to finding edges or boundaries that separate one or more target regions of interest. In this manner, an end-to-end fault detection method, FaultSeg3D [16], predicts fault probabilities directly from 3-D seismic images using the U-shaped convolutional neural network (CNN), or simply U-Net, initially developed for medical image segmentation [17]. The architecture of FaultSeg3D is displayed in Fig. 1. The input in their fault segmentation U-Net is a seismic image, and the output is the same-size fault map with value 1 indicating high probability and vice versa. The predicted fault map has a continuous value range of [0, 1]. In addition to the improved fault-detection accuracy, FaultSeg3D is also evidently computationally efficient compared with conventional attribute-based methods. Geological constraints can be used to improve the geological interpretability of U-Net fault maps [18], or different strategies can be employed to mitigate the requirement of a large training data set for fault detection on field seismic images [19], [20].

The U-Net fault segmentation has become a successful paradigm of machine learning-based automatic fault detection. However, the U-Net method can be sensitive to unknown factors in images, leading to suboptimal identification of faults. When a seismic image is noisy, the U-Net method can produce isolated, small faults with questionable geological

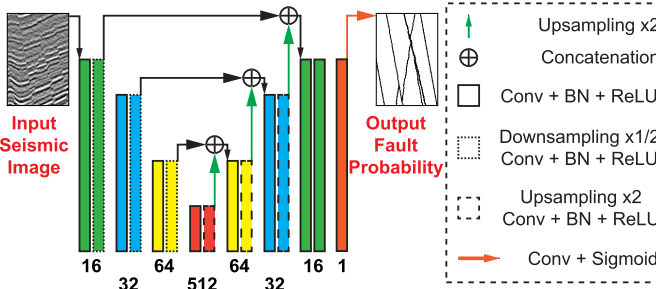


Fig. 1. Overall architecture of U-Net for fault detection [16]. The downsampling and upsampling layers use a ratio of  $2 \times 2$  in 2-D and  $2 \times 2 \times 2$  in 3-D. “BN” represents a batch normalization layer, “ReLU” represents the rectified linear unit activation layer, and “Sigmoid” represents a sigmoid activation layer [28]. The input is a seismic image, and the output is a fault probability map with a continuous value range of  $[0, 1]$  of the same size. Each encoder/decoder in U-Net consists of two consecutive convolutional layers with the same number of feature maps (denoted by the numbers below the two layers). We use slightly different styles to draw layers, concatenation, and connection arrows compared with those used in [16], but the fundamental architecture is essentially the same. We use a 2-D seismic image and a fault map in this illustration for visualization purposes.

interpretability. When undesired noises have a wavenumber spectrum magnitude and/or bandwidth similar to that of target reflectors in the image, this issue becomes even more profound. In addition, the faults predicted by the U-Net may be “fat,” that is, the predictions may suffer from suboptimal spatial resolution when predicting complex fault systems. Such deficiency may result from the fact that, in the U-Net, low-resolution contextual information is repeatedly, and to some extend unnecessarily, embedded into higher resolution feature maps caused by simple upscaling operations. Such structure may eventually lead to low-accuracy, low-resolution fault prediction, particularly when there are insufficient data fed to the neural network during training.

To improve the spatial resolution and the prediction accuracy of fault detection on seismic images, we develop a new deep learning architecture. Our new architecture is inspired by the most recent developments in image segmentation based on U-Net [21]–[24], particularly the U<sup>2</sup>-Net [24], but is significantly simplified and modified specially for seismic fault detection. Specifically, our new architecture uses a nested U-Net structure with a multiscale fusion operation to improve the accuracy and reliability of fault detection in complex and noisy seismic images. We refer to our method as the nested residual U-Net (NRU).

The encoder or the decoder in conventional U-Net consists of only simple convolutional layers. By contrast, each unit of an encoder or decoder itself in our NRU is a residual U-Net. In other words, in addition to same-level long/short skip connections that connect pairs of encoder/decoder, NRU uses multiple intrastage skip connections within each encoder and decoder. This nested deep structure avoids a direct integration of lower resolution feature maps into higher resolution feature maps. That is, in our NRU, the integration from low- to high-level features is “gradually” and “transitionally,” instead of “directly” in conventional U-Net. For the residual U-Net in each encoder/decoder, we employ one or multiple dilation convolutional kernels to improve the receptive view of the

feature maps. These dilations enable our NRU to gain a sufficiently large global view of the feature maps at each spatial resolution, a feature missing in the U-Net. Our NRU also has an effective deeper structure compared with the U-Net because of the nested architecture. It is known [25]–[27] that a deeper structure usually leads to an improved robustness to noises.

We also design a total of three resolution levels (namely, low, medium, and high spatial resolution levels) in NRU’s overall architecture. At each resolution level, we output a fault map and fuse them into a final fault map of high spatial resolution before a final convolution. In this manner, we implicitly require that the predicted fault map should be accurate at all the low-, medium-, and high-resolution levels, which eventually leads to a high-resolution fault map.

In short, we combine a nested encoder-decoder module with a multiscale fusion module in our NRU to improve fault detection. This combination enables our neural network to find long, continuous faults on seismic images, rather than picking numerous isolated or scattered small faults, particularly for noisy seismic images. Using several 2-D and 3-D synthetic images and three field seismic images, we demonstrate that our NRU provides cleaner and, therefore, more geological interpretable fault maps compared with the current state-of-the-art deep-learning-based fault detection method, U-Net [16].

This article is organized as follows. In Section II, we briefly describe the architecture of our NRU, including the three subnets in the encoders/decoders. We also describe how we train the NRU and compare its characteristics with U-Net. In Section III, we use three field data examples to demonstrate the improved fault-detection capability of our NRU compared with the state-of-the-art fault-detection U-Net. We summarize our findings in Section IV.

## II. METHODOLOGY

### A. Architecture

As a widely accepted rule in machine learning, the complexity of a neural network should be in accordance with that of the problem to solve. Otherwise, an overcomplex neural network may easily become overfitting [28] without sufficient training data, leading to problematic generalization results. Even though our neural network roots in the U<sup>2</sup>-Net [24], our studies lead to a structurally simpler and different NRU that is particularly suitable for fault identification with a limited number of training data, with its overall architecture displayed in Fig. 2.

Our NRU at its overall scale consists of a total of five encoders and decoders at three spatial resolution levels: high, medium, and low levels. The high-resolution level consists of encoder 1 and decoder 1, the medium level consists of encoder 2 and decoder 2, and the low level consists of encoder 3. In this respect, our NRU is not different from conventional U-Net, except that the latter contains fewer levels. The major difference between NRU and conventional U-Net is that each encoder or decoder in our NRU is actually an intrastage subnet, or more precisely, a residual U-Net, with their respective architectures displayed in Fig. 3(a)–(c) for encoder 1 and

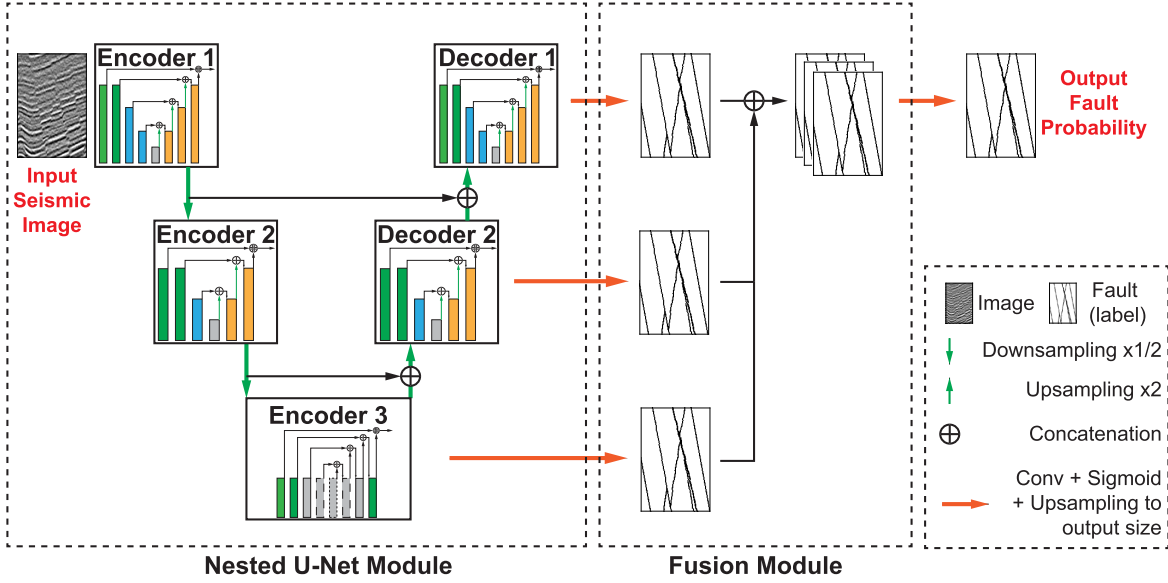


Fig. 2. Overall architecture of our NRU for fault detection. Each of the encoders/decoders is an independent residual U-Net with a respective structure shown in Fig. 3(a)–(c). The downsampling or upsampling (denoted by the downward or upward green arrows) uses a ratio of  $2 \times 2$  in 2-D and  $2 \times 2 \times 2$  in 3-D. The upsampling operation that generates an output-size layer (denoted by the red horizontal solid-line arrows) is based on bilinear interpolation in 2-D and trilinear interpolation in 3-D.

decoder 1, encoder 2 and decoder 2, and encoder 3. These residual U-Nets facilitate the entire architecture to effectively exploit intraencoder/decoder fault features, a characteristic that is missing in conventional U-Net.

The overall architecture of our NRU contains another notable difference compared with conventional U-Net NRU. In NRU, after computing a fault image at each of the three spatial resolution levels, the three fault maps of different resolutions are then linearly upsampled, concatenated, and convolved through an intermediate convolutional layer to form the final fault image after a sigmoid activation layer. Slightly different from the strategy of imposing supervisions in all levels [23], [24], we only supervise the final fault map during the training process.

We design different subnets associated with the encoders and decoders of different levels, as shown in Fig. 3. Specifically, for encoder 1 and decoder 1, we use a residual U-Net shown in Fig. 3(a), which consists of eight convolutional layers with a minimum number of 32 feature maps. In addition, this subnet has a residual connection [25] between the first convolutional encoder layer and the final decoder layer to provide better training for this nested, deep architecture. The center convolutional layer performs a two-dilated convolution. The dilational convolution enables the residual U-Net unit to gain a wider global view of the contextual information embedded in the feature maps [29]. These units are different from those in [24], where, in each of residual U-Net blocks, a fixed number of channels are used.

For encoder 2 and decoder 2, we design a simpler residual U-Net shown in Fig. 3(b), which consists of six convolutional layers plus one residual connection between the first and last layers, with a two-dilated convolutional layer connecting the encoder branch and the decoder branch. For encoder 3, the U-Net shown in Fig. 3(c) is purely convolutional without

downsampling or upsampling operations, and five out of eight convolutional layers use dilated convolution in symmetric two-, four-, eight-, four-, and two-dilation orders. The U-Net unit of encoder 3 again has a residual connection between the first and last convolutional layers. The dilational convolutions provide a different approach to feature learning for our NRU in addition to conventional downsampling/upsampling in other U-Net units.

In summary, with mathematical notations, we describe the NRU architecture as

$$\mathcal{E}_1 \in \mathbb{R}^{C_1 \times D \times H \times W} \quad (1)$$

$$\mathcal{E}_2 \in \mathbb{R}^{C_2 \times D/2 \times H/2 \times W/2} \quad (2)$$

$$\mathcal{E}_3 \in \mathbb{R}^{C_3 \times D/4 \times H/4 \times W/4} \quad (3)$$

$$\mathcal{D}_2 \in \mathbb{R}^{C_2 \times D/2 \times H/2 \times W/2} \quad (4)$$

$$\mathcal{D}_1 \in \mathbb{R}^{C_1 \times D \times H \times W} \quad (5)$$

$$F_1 = \mathcal{C}_{d=1, k=3}^{C_1 \rightarrow 1}(\mathcal{D}_1) \quad (6)$$

$$F_2 = \mathcal{W}_{k=2}(\mathcal{C}_{d=1, k=3}^{C_2 \rightarrow 1}(\mathcal{D}_2)) \quad (7)$$

$$F_3 = \mathcal{W}_{k=4}(\mathcal{C}_{d=1, k=3}^{C_3 \rightarrow 1}(\mathcal{E}_3)) \quad (8)$$

$$F = \sigma(\mathcal{C}_{d=1, k=1}^{3 \rightarrow 1}(F_1 \oplus F_2 \oplus F_3)) \quad (9)$$

where  $\mathcal{E}_i$  represents the feature maps of the  $i$ th encoder,  $\mathcal{D}_i$  represents the feature maps of the  $i$ th decoder,  $F_i \in \mathbb{R}^{1 \times D \times H \times W}$  with  $i = 1, 2, 3$  are three intermediate fault maps at different spatial scales,  $F \in \mathbb{R}^{1 \times D \times H \times W}$  is the final fault map, and  $D$ ,  $H$ , and  $W$  indicate the dimensions of the input (and the output). The number of output feature maps associated with the encoders are  $C_1 = 32$ ,  $C_2 = 64$ , and  $C_3 = 16$ , respectively. The convolutional layer  $\mathcal{C}_{d=n, k=m}^{l \rightarrow h}$  represents a convolutional layer with a kernel size of  $m \times m \times m$  with a dilation of  $n$ ,  $l$  input feature maps, and  $h$  output feature maps.  $\mathcal{W}_{k=n}$  represents a linear upsampling (i.e., bilinear upsampling in 2-D or trilinear upsampling in 3-D) of ratio  $n$ .

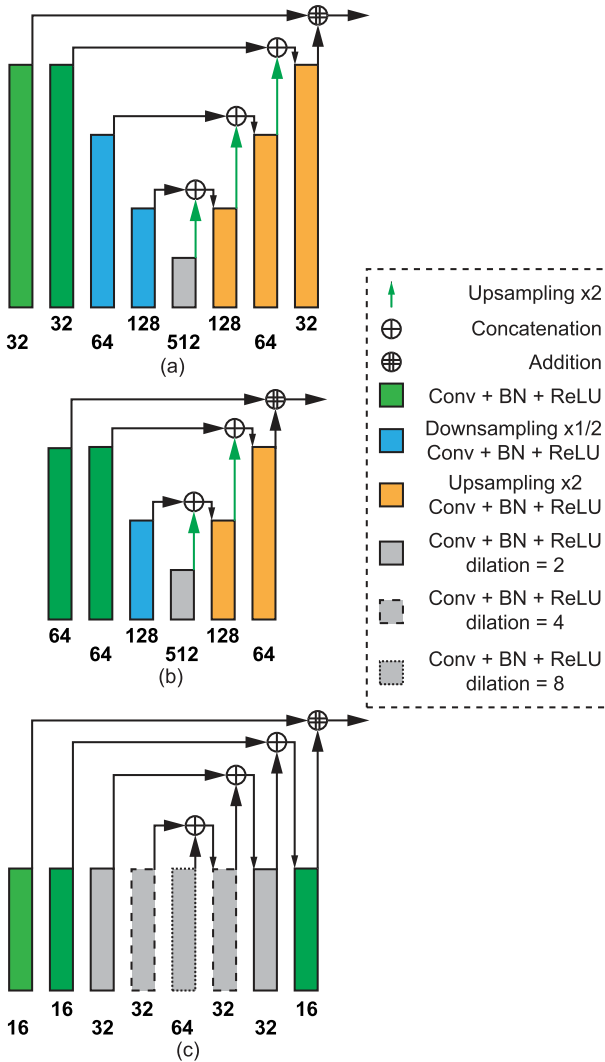


Fig. 3. Architectures of intrastage subnets in our NRU. (a) Subnet associated with encoder 1 and decoder 1. (b) Subnet associated with encoder 2 and decoder 2. (c) Subnet associated with encoder 3. The numbers below the layers represent the number of feature maps within each convolutional layer. All the convolutional layers in the subnets use a kernel size of  $3 \times 3$  in 2-D and  $3 \times 3 \times 3$  in 3-D.

$\sigma$  represents the sigmoid activation function, and  $\oplus$  represents concatenation of two feature maps.

Meanwhile, the encoders and decoders can be expressed as

$$\mathcal{I}_1 = \mathcal{R}(\mathcal{C}_{d=1, k=3}^{1 \rightarrow 32}(I)) \quad (10)$$

$$\mathcal{E}_1 = \mathcal{I}_1 + \mathcal{U}_{1,1,1,2,1,1,1}^{32 \rightarrow 64 \rightarrow 128 \rightarrow 512 \rightarrow 128 \rightarrow 64 \rightarrow 32}(\mathcal{I}_1) \quad (11)$$

$$\mathcal{I}_2 = \mathcal{R}(\mathcal{C}_{d=1, k=3}^{32 \rightarrow 64}(\mathcal{M}_2(\mathcal{E}_1))) \quad (12)$$

$$\mathcal{E}_2 = \mathcal{I}_2 + \mathcal{U}_{1,1,2,1,1}^{64 \rightarrow 128 \rightarrow 512 \rightarrow 128 \rightarrow 64}(\mathcal{I}_2) \quad (13)$$

$$\mathcal{I}_3 = \mathcal{R}(\mathcal{C}_{d=1, k=3}^{64 \rightarrow 16}(\mathcal{M}_2(\mathcal{E}_2))) \quad (14)$$

$$\mathcal{E}_3 = \mathcal{I}_3 + \mathcal{U}_{1,2,4,8,4,2,1}^{16 \rightarrow 32 \rightarrow 32 \rightarrow 64 \rightarrow 32 \rightarrow 32 \rightarrow 16}(\mathcal{I}_3) \quad (15)$$

$$\mathcal{I}_4 = \mathcal{R}(\mathcal{C}_{d=1, k=3}^{16+64 \rightarrow 64}(\mathcal{E}_2 \oplus \mathcal{W}_2(\mathcal{E}_3))) \quad (16)$$

$$\mathcal{D}_2 = \mathcal{I}_4 + \mathcal{U}_{1,1,2,1,1}^{64 \rightarrow 128 \rightarrow 512 \rightarrow 128 \rightarrow 64}(\mathcal{I}_4) \quad (17)$$

$$\mathcal{I}_5 = \mathcal{R}(\mathcal{C}_{d=1, k=3}^{64+32 \rightarrow 32}(\mathcal{E}_1 \oplus \mathcal{W}_2(\mathcal{D}_2))) \quad (18)$$

$$\mathcal{D}_1 = \mathcal{I}_5 + \mathcal{U}_{1,1,1,2,1,1,1}^{32 \rightarrow 64 \rightarrow 128 \rightarrow 512 \rightarrow 128 \rightarrow 64 \rightarrow 32}(\mathcal{I}_5) \quad (19)$$

where  $I \in \mathbb{R}^{1 \times D \times H \times W}$  is the input seismic image,  $\mathcal{I}_i$  with  $i = 1, \dots, 5$  is intermediate input of each encoder/decoder block, and  $\mathcal{U}_{m,n,\dots,p,\dots,n,m}^{a \rightarrow b \rightarrow \dots \rightarrow c \rightarrow \dots \rightarrow b \rightarrow a}$  represents a U-Net structure with  $a, b, \dots, c, \dots, b, a$  being output feature maps in the convolutional layers, with proper maxpooling, upsampling, and concatenation connecting these convolutional layers. We use right-pointed horizontal arrows over the numbers of feature maps to indicate the skip connections. The subscripts represent  $m-, n-, \dots, p-, \dots, n-, m$ -dilated convolutions associated with these convolutional kernels.  $\mathcal{M}_2$  represents a maxpooling layer with downsampling ratio 2, while  $\mathcal{W}_2$  represents linear upsampling of ratio 2.  $\mathcal{R}$  represents the ReLU activation function. The residual connections of these residual U-Net units are represented by the  $+$  symbol between the input and the U-Net output. As discussed previously, the residual U-Net at the lowest spatial scale, i.e., (15), does not use any maxpooling or upsampling.

By contrast, the conventional U-Net for fault segmentation [16] is

$$\mathcal{I} = \mathcal{U}_1^{16, 16 \rightarrow 32, 32 \rightarrow 64, 64 \rightarrow 512, 512 \rightarrow 64, 64 \rightarrow 32, 32 \rightarrow 16, 16}(I) \quad (20)$$

$$F = \sigma(\mathcal{C}_{d=1, k=1}^{16 \rightarrow 1}(\mathcal{I})) \quad (21)$$

where a single subscript 1 for  $\mathcal{U}$  represents that all the convolutional layers in the U-Net are one-dilated convolutions. Again,  $I, F \in \mathbb{R}^{1 \times D \times H \times W}$ . Generally, the U-Net adopts a dual layer scheme in an encode or a decoder, which is represented by the repeated numbers of feature maps, e.g., 16, 16. It is worth noting that, in both the residual U-Net blocks and the U-Net, the decoder branch accepts concatenations from the encoder branch; therefore, the number of input feature maps in the decoder branch is the summation of that from the encoder and that of a decoder [16], [17].

### B. Loss Function, Training, and Validation

The loss function plays a critical role in machine learning to ensure a converged training and proper generalization [28], [30]. To improve convergence, we use a smoothed dice loss function [31] as follows:

$$\mathcal{L} = 1 - \frac{2 \sum_{i=1}^N y_i p_i + 1}{\sum_{i=1}^N y_i + \sum_{i=1}^N p_i + 1} \quad (22)$$

where  $y_i$  is the ground truth with values 0 or 1 (indicating nonfault or fault in a provided fault label) of the  $i$ th image pixel,  $p_i$  is the predicted fault probability value of the  $i$ th image pixel, with a value range of  $0 \leq p_i \leq 1$ , and  $N$  is the total number of pixels in the image. Our trial and error tests find that the dice loss is particularly suitable to our fault detection task.

The training of our NRU requires a set of seismic images and associated fault labels. We train the 2-D version and 3-D version of our NRU separately. For 3-D NRU training and validation, we adopt an open-source seismic image data set provided by Wu *et al.* [16]. The data set contains a total of 200 3-D synthetic seismic images with their associated fault labels.

Each seismic image (and its fault label) has a dimension of  $128 \times 128 \times 128$ . To augment the data set, we flip each of the 200 images/faults with respect to the  $x_1, x_2, x_3, x_1+x_2, x_1+x_3, x_2+x_3$ , and  $x_1+x_2+x_3$  axis/axes. Therefore, the final 3-D training data set consists of a total of 1600 seismic images and their fault labels. We use a total of 160 seismic images/fault labels as the validation data set, of which 20 are from the original 3-D validation data set and 140 are augmented by flipping as in the training data augmentation. The validation data set has no overlapping with the training data set to ensure an unbiased validation.

For 2-D NRU training and validation, we create a training data set and a validation data set from an open-source synthetic 3-D seismic image data set. We randomly slice a total of 1000 2-D seismic images from these 3-D seismic image volumes and their fault labels and augment the images by flipping them with respect to the  $x_1, x_2$ , and  $x_1+x_2$  axis/axes. The final training data set, thus, contains a total of 4000 synthetic 2-D seismic images and their corresponding fault labels. These synthetic images are prepared with different levels of random noises to facilitate a robust generalization. We create a validation data set that contains 400 synthetic 2-D seismic images and their fault labels in a similar manner. Again, the validation data set does not overlap with the training data set.

The 2-D and 3-D versions of our NRU share the same architecture; except that, for 3-D fault detection, the input/output and all the convolutional, downsampling, upsampling, concatenation, and residual summation operations are replaced with their corresponding 3-D operations.

To ensure an unbiased comparison between our NRU and the U-Net method [16] in the numerical examples, we implement both the 2-D and 3-D U-Net and our NRU using PyTorch [32] accompanied with distributed training provided by PyTorch Lightning [33] and train the two neural networks using the Adam optimization [28]. The batch size of the 2-D training is 8, while that of the 3-D training is 16, partially for training efficiency purposes. The learning rate is automatically reduced by a factor of 10 every 25 epochs, with an initial learning rate of  $10^{-4}$ . The U-Net implementations closely follow the paradigm in [16]. Fig. 4 display the loss convergence history of our 3-D NRU training and validation, which indicates that our NRU architecture is suitable for our fault detection task.

To qualitatively compare the fault prediction capabilities of our NRU with those of conventional U-Net, we show in Fig. 5 a series of fault identification on synthetic seismic images selected from the validation data set. The eight rows in Fig. 5 represent different synthetic seismic images with different levels of random noise. The four columns in Fig. 5 represent the seismic images, the ground-truth faults, the faults identified by U-Net, and those identified by our NRU, respectively. The fault maps produced by the U-Net in the first four rows are generally consistent with the ground-truth fault maps. However, the detected faults are visibly “fat,” resulting in some level of uncertainties in interpreting those faults. By contrast, our NRU produces four fault maps that are almost identical to the ground-truth faults with high spatial resolution.

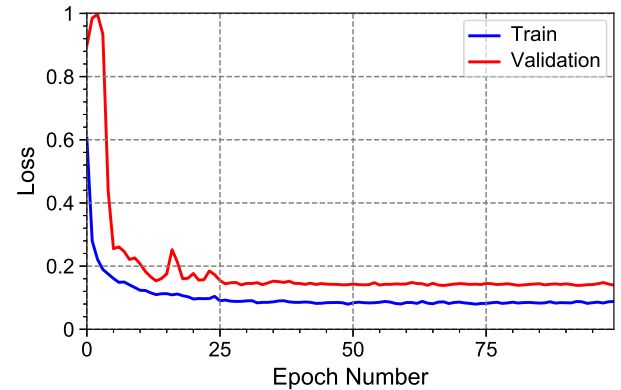


Fig. 4. Hybrid losses associated with the training (blue) and the validation (red) of our 3-D NRU.

The fault maps produced by the U-Net in the bottom four rows show visible inconsistencies compared with the ground-truth faults—some predicted faults are broken (the fifth and seventh rows), while some are erroneous detection (the sixth and eighth rows). In comparison, our NRU predictions are almost identical to the ground truth, manifesting the excellent capability of NRU in delineating complex faults.

To evaluate the robustness of our NRU to noises, we show in Fig. 6 a comparison between U-Net and our NRU for fault detection on a synthetic seismic image with added random noises of different maximum magnitudes. This synthetic image is not in the training data set. Similar to Fig. 5, the four columns in Fig. 6 represent the images, the ground-truth faults, the faults detected using U-Net, and our NRU, respectively. Notably, even in the fifth and sixth rows, our NRU still produces several faults that resemble some of the ground-truth faults, while U-Net produces a fault map with many random, isolated, artificial “faults.” In the seventh row where the seismic image is severely contaminated by random noises, it is visually impossible to pick any faults. For this image, U-Net produces a fault map with almost completely uninterpretable faults, while our NRU still identifies two or three faults that are close to the ground truth, though with some biases.

These results indicate that our NRU is more robust to noises in the image—when the image is severely contaminated by unknown factors, such as random noises, our NRU can avoid misidentification of some ambiguous image features like faults, a characteristic that is opposite to that of U-Net. This advantage results from the unique architecture of NRU. This comparison implies that, for field seismic images, our NRU method has great potential to produce a cleaner fault map with less misdetection compared with the U-Net method.

We further verify the efficacy and accuracy of our NRU on a 3-D noisy synthetic seismic image selected from the validation data set shown in Fig. 7. Fig. 7(a)–(c) displays the ground-truth faults, the faults predicted by U-Net, and those predicted by our NRU, respectively, overlying on this seismic image. Visually, both U-Net and our NRU produce fault maps with high fault probability. However, our NRU predicted faults are relatively “sharper” than the U-Net predicted faults at fault-background interfaces. In other words, the faults in Fig. 7(c) have a relatively higher probability and fewer

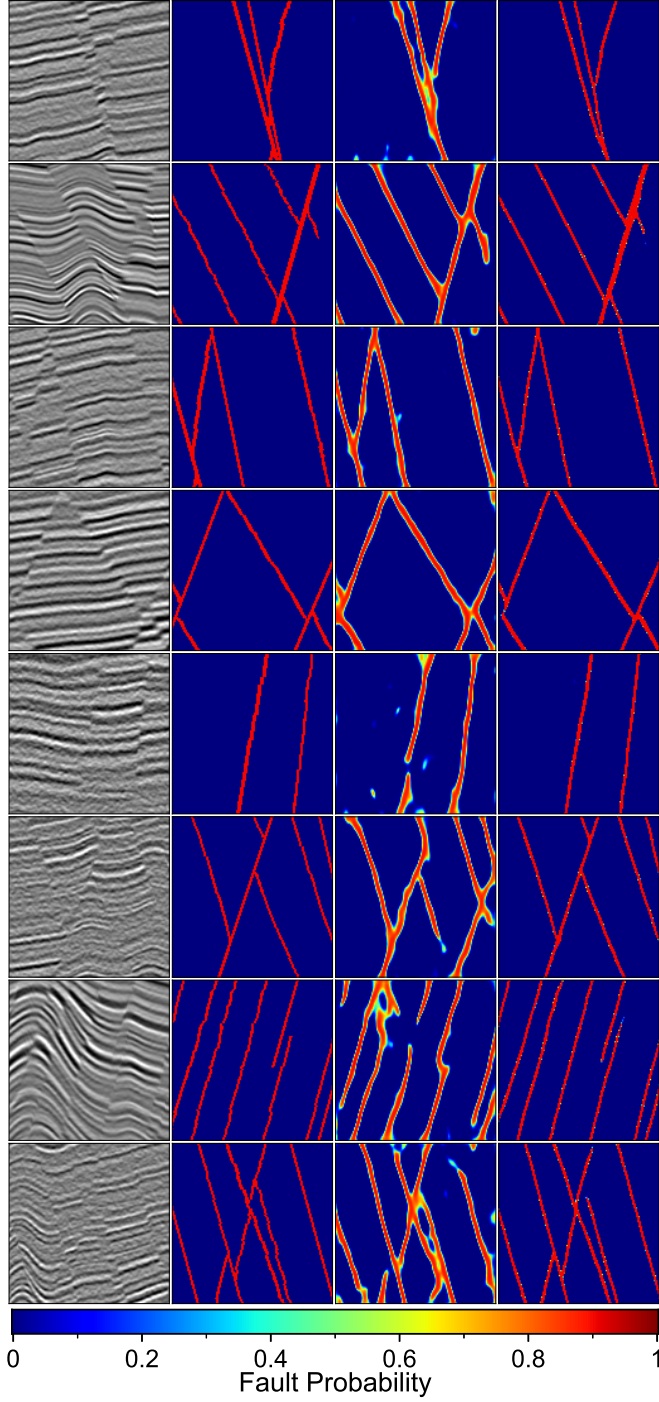


Fig. 5. Comparisons between the identified faults obtained using U-Net and our NRU for synthetic seismic images that are not in the training data set. Rows 1–8 represent eight different seismic images with different numbers of faults. Columns 1–4 represent: 1) seismic migration images; 2) the true faults; 3) the faults detected by U-Net; and 4) the faults detected by our NRU, respectively.

uncertainties than those in Fig. 7(b). Similarly, we compare among the ground-truth faults, the U-Net-generated faults, and our NRU-generated faults in Fig. 8 for another 3-D noisy synthetic image in the validation data set. This comparison resembles that in Fig. 7, indicating that our NRU produces

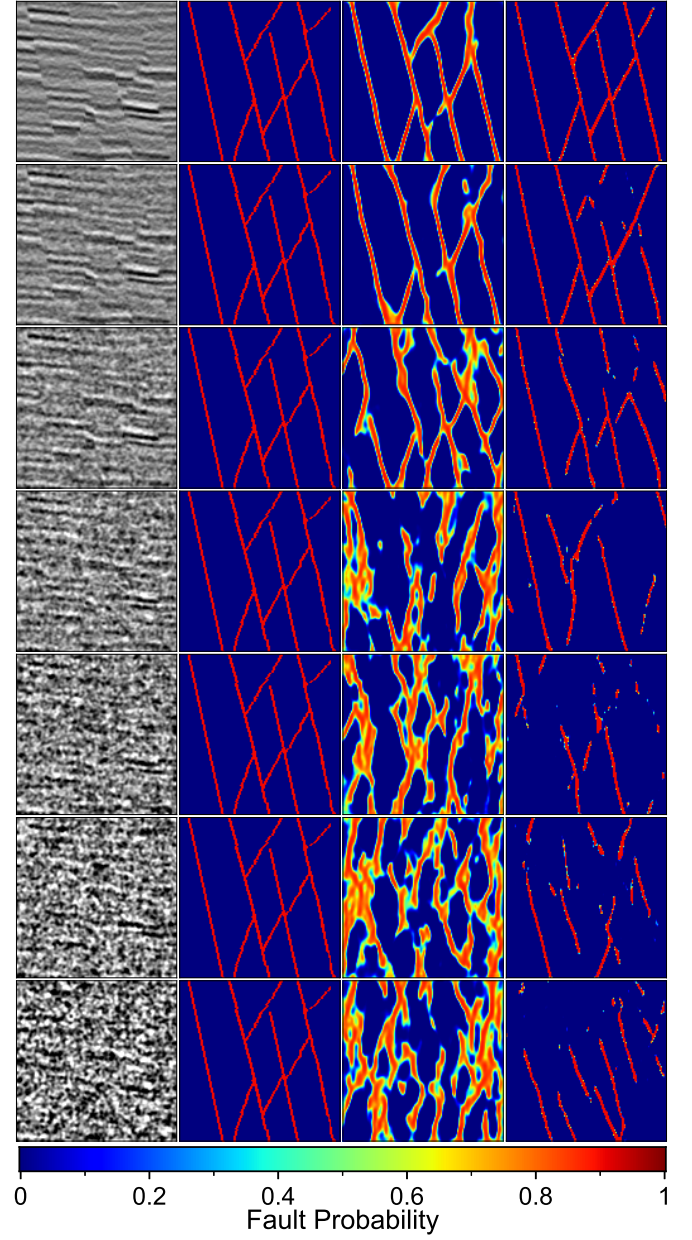


Fig. 6. Comparisons among faults identified using U-Net and our NRU for the same synthetic seismic image with added low to high levels of random noise. The synthetic image is not in the training data set. Rows 1–7 correspond to the seismic images with different levels of random noise. Columns 1–4 represent: 1) the noisy seismic images; 2) the ground-truth faults; 3) the faults detected by U-Net; and 4) the faults detected by our NRU, respectively.

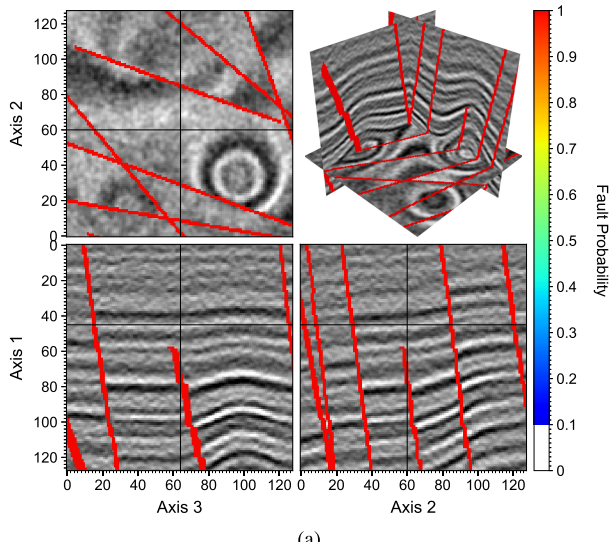
sharper faults with a relatively higher probability compared with U-Net.

### III. NUMERICAL EXAMPLES

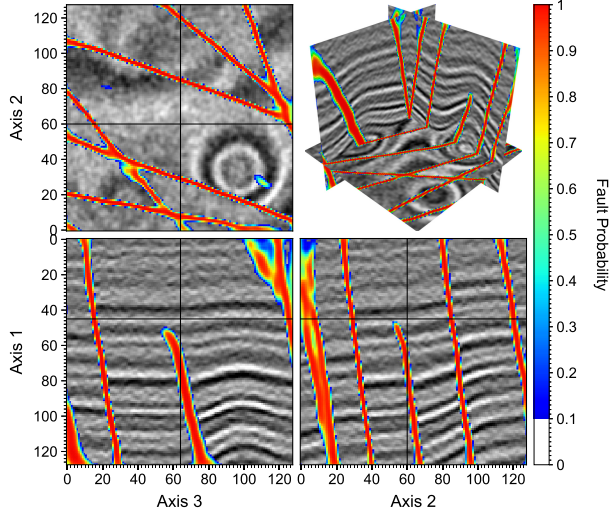
We use three field seismic images to demonstrate the excellent fault detection capability of our NRU over the current state-of-the-art architecture, U-Net.

#### A. Utah FORGE Image

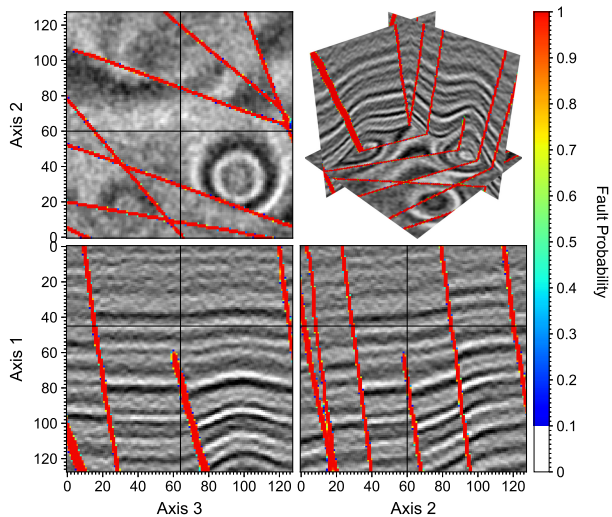
In the first example, we use a 2-D land field seismic image, provided as open data by the Energy and Geoscience Institute,



(a)

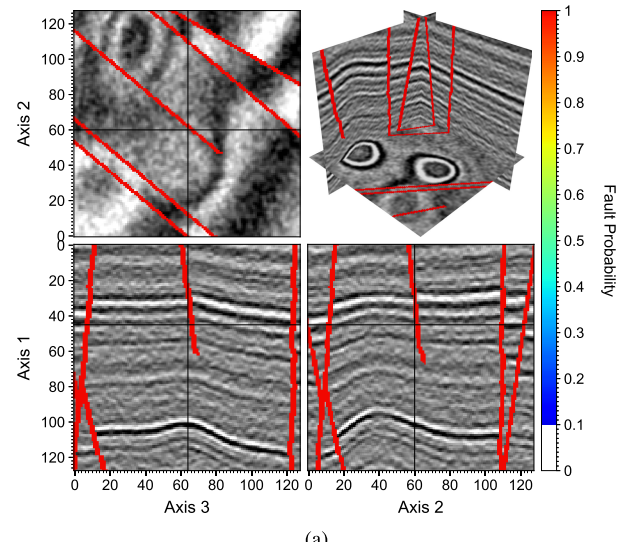


(b)

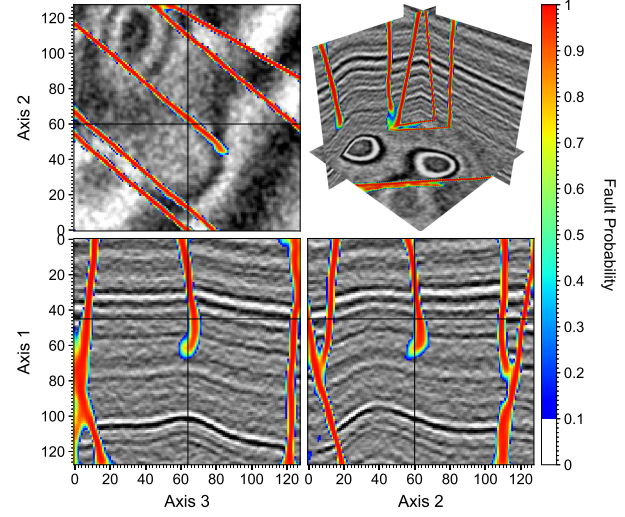


(c)

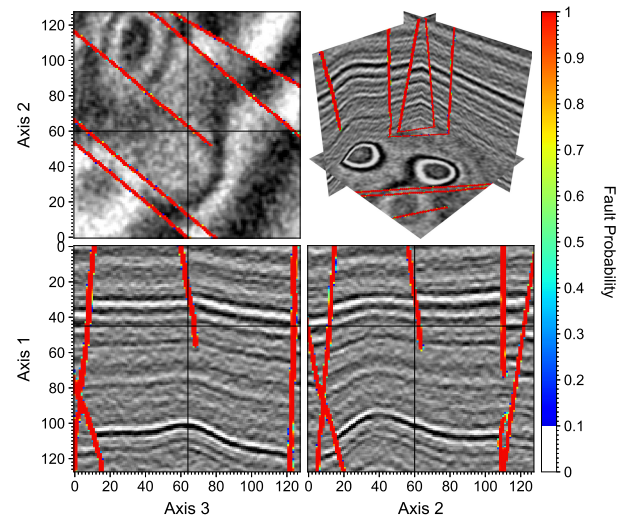
Fig. 7. (a) Ground-truth faults overlying on the corresponding 3-D seismic image. (b) Faults predicted by U-Net. (c) Faults predicted by our NRU.



(a)

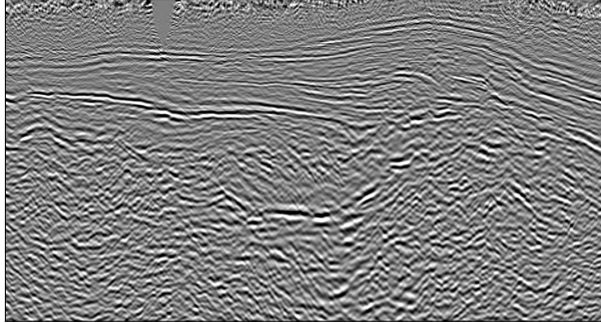


(b)

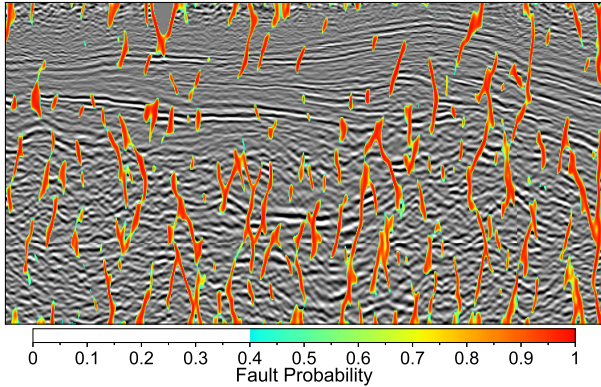


(c)

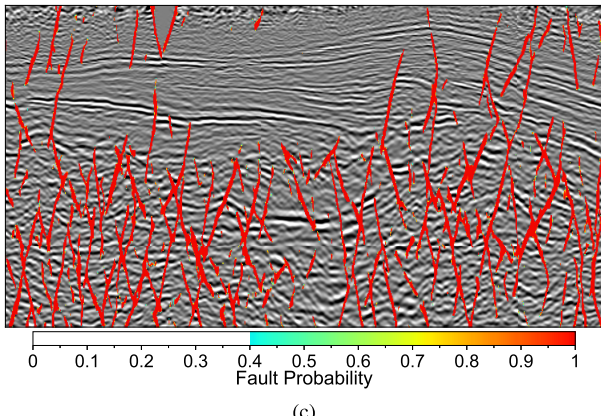
Fig. 8. (a) Ground-truth faults overlying on the corresponding 3-D seismic image. (b) Faults predicted by U-Net. (c) Faults predicted by our NRU.



(a)



(b)



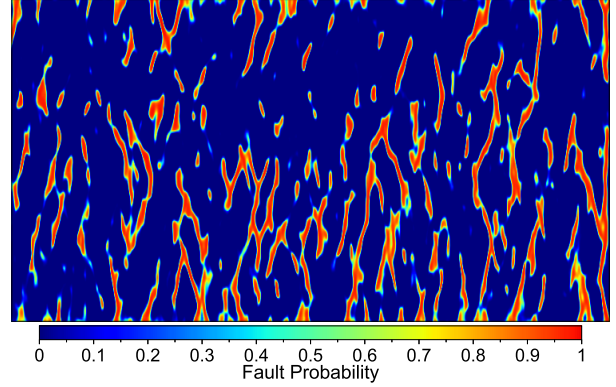
(c)

Fig. 9. (a) Seismic image of a 2-D land seismic survey line at the Utah FORGE project site. (b) Faults detected by U-Net overlying on the image. (c) Faults detected by our NRU overlying on the image.

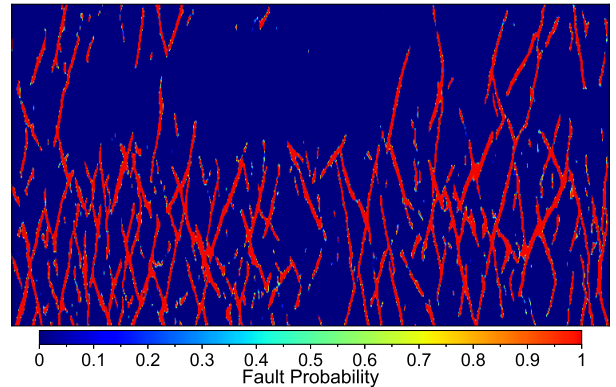
The University of Utah, for the Utah FORGE geothermal project [34], to demonstrate the improved fault-detection capability of our NRU over U-Net.

Fig. 9 displays the 2-D prestack depth migration image at the Utah FORGE project site. The image is sampled by 256 grid points in the vertical direction and 730 grid points in the horizontal direction. The shallow region of the image shows a number of reflectors, but the deep region of the image has a fairly low signal-to-noise ratio and is full of broken reflectors, preventing an easy, definitive fault picking by seismic interpreters.

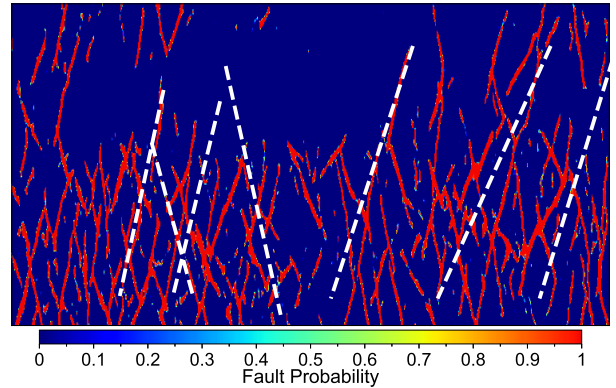
We first use U-Net to predict faults on this image and show the resulting fault map in Fig. 9(b) superimposed onto the image and in Fig. 10(a) separately. We observe that U-Net does detect most of the visible reflector discontinuities with high



(a)



(b)



(c)

Fig. 10. (a) Fault probability map produced using U-Net for a 2-D seismic image at the Utah FORGE project site. (b) Fault probability map produced using our NRU. (c) NRU-produced fault probability map shown in (b), superimposed with a tentative geological interpretation by hand drawing based on the fault distribution. White dashed lines indicate interpreted, possible major faults or fault zones.

fault probabilities. However, the resulting fault map contains too numerous interlacing faults, short or long, to make itself geologically plausible. This geologically excessive fault map indicates that the fault detection using U-Net is severely deteriorated by the imperfect imaging caused by several factors, such as insufficient data coverage or stacking, and/or image artifacts, and/or other unknown image noises. The result in Fig. 9(b) resembles what is observed in the third column of Fig. 6.

We then use our NRU to detect faults on this UTAH FORGE seismic image and show the results in Figs. 9(c) and 10(b).

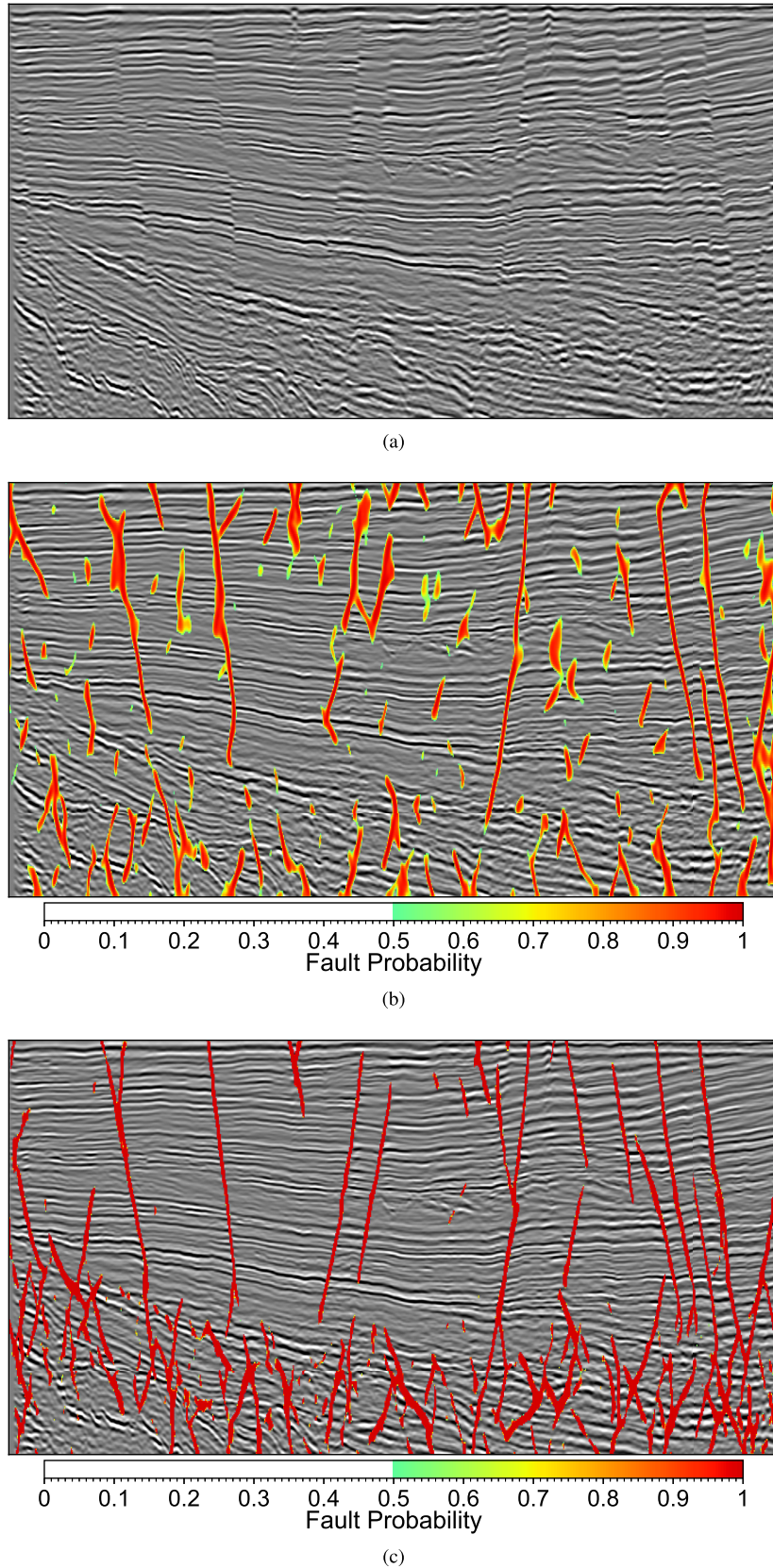


Fig. 11. (a) 2-D slice from the New Zealand Kerry 3-D image. (b) Faults detected by U-Net overlying on the image. (c) Faults detected by our NRU overlying on the image.

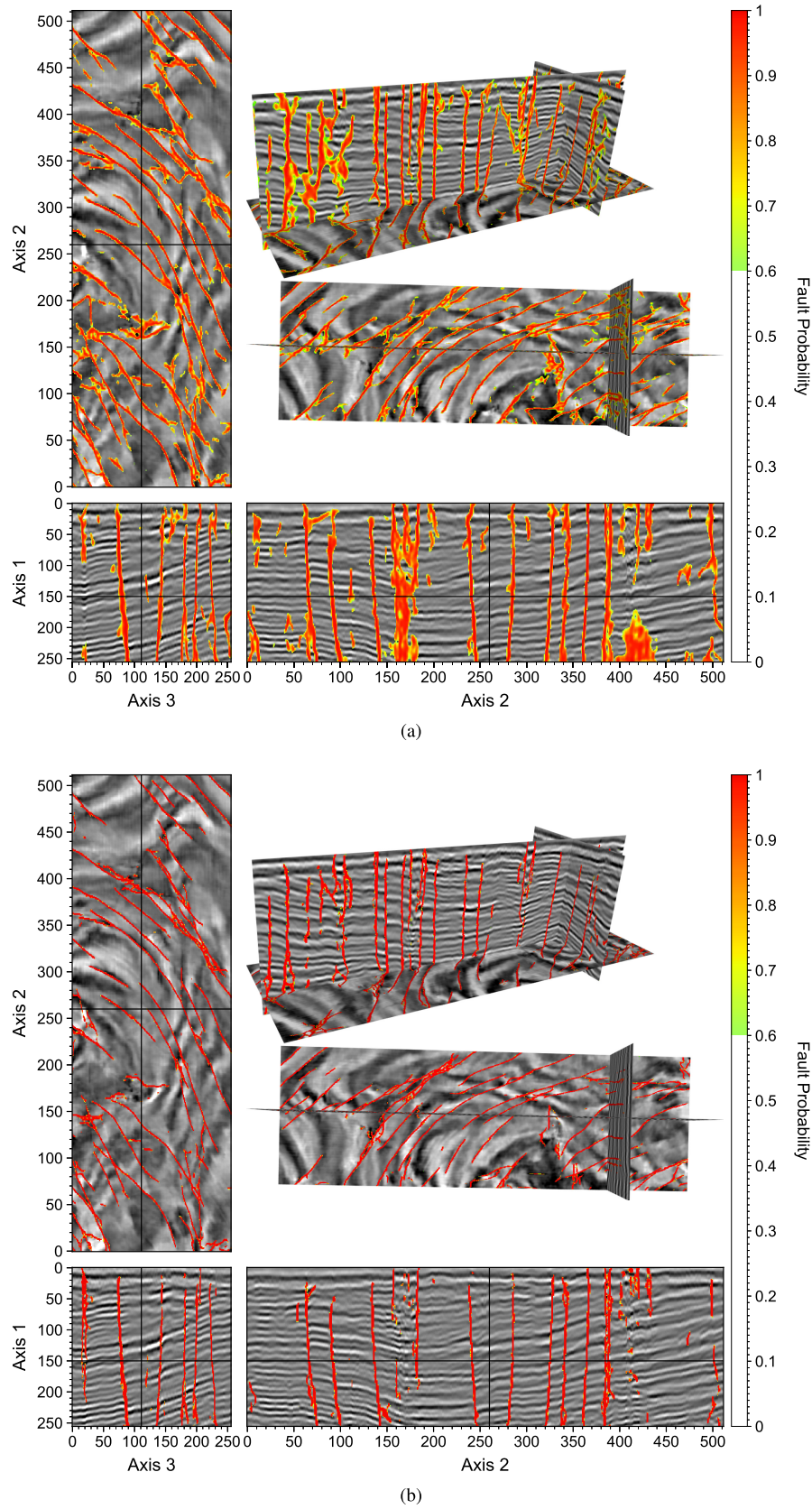


Fig. 12. Portion of the Kerry 3-D image volume superimposed with the faults predicted using (a) U-Net and (b) our NRU.

It is obvious that the NRU fault map contains fewer, yet more definitive and interpretable, faults. Almost all NRU detected faults are clearly associated with lateral reflector

discontinuities on the image, indicating that they are indeed identified based on the discontinuity features on the seismic structural image. Our NRU detected faults indicate that the

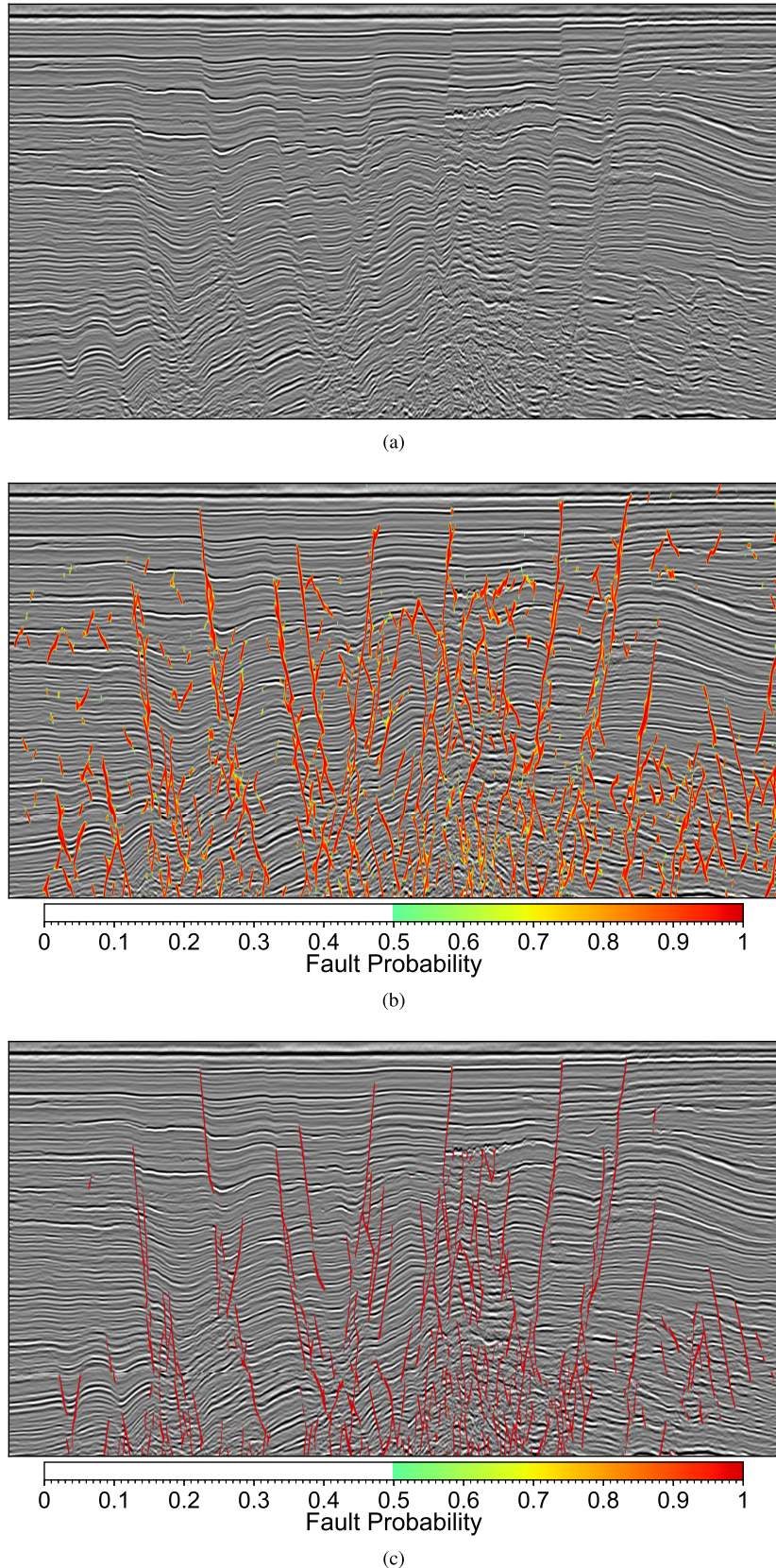


Fig. 13. (a) 2-D slice of the New Zealand Opunake 3-D image. (b) Faults detected using the U-Net overlying on the image. (c) Faults detected using our NRU overlying the image.

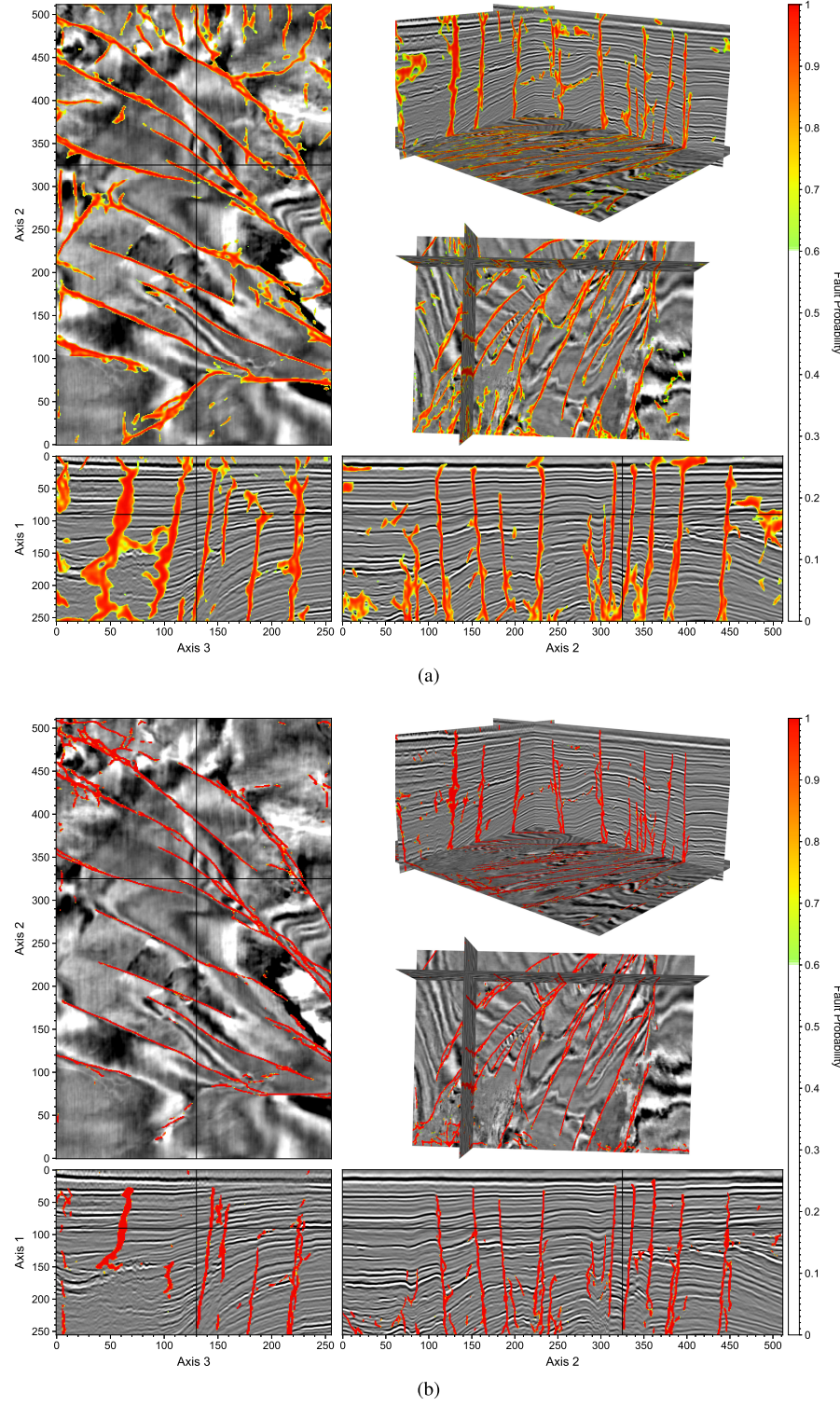


Fig. 14. Part of the Opunake 3-D image volume superimposed with the faults predicted using (a) U-Net and (b) our NRU.

region contains a fault system consisting of a rich set of small-to medium-scale faults. With some level of uncertainty, we plot a tentative sketch of this fault system in Fig. 10(c) using white dashed lines. By contrast, it is almost impossible for us to identify such a system on the U-Net fault map in Fig. 10(a). This numerical example further demonstrates the excellent

fault identification capability of our NRU compared with the current state-of-the-art fault detection method based on U-Net.

#### B. Kerry Image

In the second example, we demonstrate the efficacy and accuracy of our NRU and compare the fault prediction result

with that produced using U-Net, on a 3-D field seismic image provided as open data by the Society of Exploration Geophysicists (SEG) [35].

We first test on a 2-D slice [see Fig. 11(a)] of this 3-D image. The 2-D slice is sampled by 256 grid points in the vertical direction and 730 grid points in the horizontal direction. We perform a 2-D windowed root-mean-square balance with a window size of 25 grid points in both dimensions. Visually, there exist several major faults with deep penetrating depth in this image.

We perform fault detection using U-Net and our NRU and show the resulting fault maps in Fig. 11(b) and (c), respectively. Both U-Net and our NRU find most of the major faults in the image. However, we observe that several major faults in the U-Net fault map in Fig. 11(b) are more broken compared with our NRU result in Fig. 11(c). For instance, our NRU detects up to ten major faults in the image, all with continuous paths and high dip angles, which are somewhat broken in the U-Net fault map. Particularly, the U-Net misses two parallel major faults in the center of the image and two or three medium-length faults on the right of the image. The U-Net's prediction also appears to contain a large number of small, isolated faults that lack clearly identifiable dominant orientation. The prediction is, therefore, difficult to interpret using a reasonable geological model. By contrast, our NRU prediction is more geological interpretable because of the improved continuity of fault paths. In the lower part of the image where the signal-to-noise ratio is relatively lower, the U-Net's prediction seems to be insufficient by missing numerous subtle faults. By contrast, our NRU delineates more faults. A careful review of these faults indicates that they correspond well with lateral reflector discontinuities.

This comparison demonstrates that, compared with U-Net, our NRU tends to produce a geologically more interpretable fault map for this field seismic image and avoid overdetection of small-scale faults.

We further validate the accuracy of our NRU for 3-D fault detection using a portion of the 3-D Kerry image. We show the detected faults overlying on the 3-D image in Fig. 12. Fig. 12(a) displays the faults detected using the U-Net, while Fig. 12(b) displays those detected using our NRU. In general, the detected faults have fairly similar spatial locations on the two fault maps, and both fault maps exhibit high fault probabilities at the detected faults. Nevertheless, we find that the faults predicted by U-Net have relatively higher uncertainties (lower fault probabilities) around the faults compared with our NRU prediction in Fig. 12(b)—almost all the faults in our NRU prediction have a high fault probability close to 1. The higher fault probability in our NRU enables us to identify two spatially close, quasi-parallel faults from the image volume, such as those at approximately  $x_2 = 385$  on the  $x_1-x_2$  plane, while, on the U-Net prediction fault map, these two faults can barely be identified.

### C. Opunake Image

In the third example, we compare the fault-detection results produced using U-Net and our NRU on another field data

seismic image, the New Zealand Opunake 3-D image, an open image volume provided by SEG [36].

We again slice the 3-D image and obtain a 2-D image shown in Fig. 13(a). The 2-D image is sampled by 591 grid points in the vertical direction and 2001 grid points in the horizontal direction. We detect a normal fault system on this image. Fig. 13(b) displays the faults detected using U-Net. The U-Net detects numerous small, scattered faults distributed in the entire image, some with a fairly limited length and a clustered distribution pattern. By contrast, Fig. 13(c) displays the detected faults using our NRU. The fault map is visually cleaner compared with that in Fig. 13(b) produced using U-Net. Most faults predicted using our NRU have more definitive, continuous, and high-resolution paths compared with those in Fig. 13(b). In addition to the fact that all the major faults are clearly revealed, smaller-scale faults, such as those near the center of the image, are also easier to interpret geologically compared with those at the same region in Fig. 13(b). These results show that our NRU successfully avoids overidentification of faults on this field seismic image, leading to better geological interpretability compared with U-Net.

We further validate the accuracy of our NRU for 3-D fault detection using the upper part of the 3-D Opunake image. We show the detected faults overlying on the 3-D image in Fig. 14. Fig. 14(a) displays the faults detected using the state-of-the-art U-Net, while Fig. 14(b) displays those detected using our NRU. The detected faults have fairly similar spatial locations on the two fault maps. However, we find that the faults predicted by U-Net have relatively higher uncertainties (lower fault probabilities) around the faults compared with our NRU prediction in Fig. 14(b). In the NRU-predicted fault map, almost all the faults in our NRU prediction have a high fault probability close to 1. As a result, our NRU seems to better resolve some faults that are close to each other. For example, on the horizontal slice ( $x_2-x_3$  plane), we find that our NRU resolves a set of closely developed faults with high resolution in the range of  $x_2 = 200 \sim 300$  and  $x_3 = 150 \sim 250$ , while, on the U-Net fault map, these detected faults smear into each other because of insufficient spatial resolution. On the vertical slices ( $x_1-x_2$  and  $x_1-x_3$  planes), the faults on the NRU fault map appear to be of higher resolution in the horizontal direction compared with those predicted by the U-Net, which facilitates more definitive seismic interpretation.

## IV. CONCLUSION

We have developed an automatic, end-to-end fault identification method using a nested residual U-shaped CNN. The most distinct feature of this neural network compared with the current state-of-the-art method, U-Net-based fault detection, is that each of the encoders and decoders is a residual U-Net that exploits intraencoder/decoder fault features. In addition, we use a fusion operation to combine the fault maps from three different spatial resolution scales in the neural network to produce the final fault map. Therefore, our neural network has a nested fusion structure. We demonstrate the excellent fault detection capability and improved robustness to image

noises of our new neural network through several synthetic and field seismic images. We find that our method produces notably cleaner and more interpretable fault maps compared with the conventional U-Net fault detection, which may benefit automatic seismic interpretation.

#### ACKNOWLEDGMENT

The Los Alamos National Laboratory (LANL) is operated by Triad National Security, LLC, for the U.S. DOE National Nuclear Security Administration (NNSA) under Contract 89233218CNA000001. This research used computing resources provided by the LANL Institutional Computing Program supported by the U.S. DOE NNSA. The authors thank Xinming Wu for open-sourcing his pioneering FaultSeg3D and associated data sets, which make it possible for us to adopt the high-quality data set to train our neural network. They thank S. Mostafa Mousavi and Haibin DI for their careful and insightful comments that greatly improve this article.

#### REFERENCES

- [1] P. Avseth, T. Mukerji, and G. Mavko, *Quantitative Seismic Interpretation: Applying Rock Physics Tools to Reduce Interpretation Risk*. Cambridge, U.K.: Cambridge Univ. Press, 2005.
- [2] H. Fossen, *Structural Geology*, 2nd ed. Cambridge, U.K.: Cambridge Univ. Press, 2016.
- [3] Q. Gan and D. Elsworth, "Analysis of fluid injection-induced fault reactivation and seismic slip in geothermal reservoirs," *J. Geophys. Res., Solid Earth*, vol. 119, no. 4, pp. 3340–3353, Apr. 2014, doi: [10.1002/2013JB010679](https://doi.org/10.1002/2013JB010679).
- [4] K. Gao, L. Huang, and T. Cladouhos, "Three-dimensional seismic characterization and imaging of the soda lake geothermal field," *Geothermics*, vol. 90, Feb. 2021, Art. no. 101996. [Online]. Available: <https://www.sciencedirect.com/science/article/pii/S0375650520302881>
- [5] V. Vilarrasa and J. Carrera, "Geologic carbon storage is unlikely to trigger large earthquakes and reactivate faults through which CO<sub>2</sub> could leak," *Proc. Nat. Acad. Sci. USA*, vol. 112, no. 19, pp. 5938–5943, May 2015. [Online]. Available: <https://www.pnas.org/content/112/19/5938>
- [6] R. F. P. Hardman and J. E. Booth, "The significance of normal faults in the exploration and production of north sea hydrocarbons," *Geological Soc., London, Special Publications*, vol. 56, no. 1, pp. 1–13, 1991. [Online]. Available: <https://sp.lyellcollection.org/content/56/1/1>
- [7] K. J. Marfurt, R. L. Kirlin, S. L. Farmer, and M. S. Bahorich, "3-D seismic attributes using a semblance-based coherency algorithm," *Geophysics*, vol. 63, no. 4, pp. 1150–1165, 1998, doi: [10.1190/1.1444115](https://doi.org/10.1190/1.1444115).
- [8] K. J. Marfurt, V. Sudhaker, A. Gerstenkorn, K. D. Crawford, and S. E. Nissen, "Coherency calculations in the presence of structural dip," *Geophysics*, vol. 64, no. 1, pp. 104–111, Jan. 1999, doi: [10.1190/1.1444508](https://doi.org/10.1190/1.1444508).
- [9] X. Wu, "Directional structure-tensor-based coherence to detect seismic faults and channels," *Geophysics*, vol. 82, no. 2, pp. A13–A17, Mar. 2017, doi: [10.1190/geo2016-0473.1](https://doi.org/10.1190/geo2016-0473.1).
- [10] P. Bakker, "Image structure analysis for seismic interpretation," Ph.D. dissertation, Delft Univ. Technol., Delft, The Netherlands, 2002.
- [11] S. I. Pedersen, T. Randen, L. Sonnenland, and O. Steen, "Automatic fault extraction using artificial ants," in *Proc. SEG Tech. Program Expanded Abstr.*, 2005, pp. 512–515, doi: [10.1190/1.1817297](https://doi.org/10.1190/1.1817297).
- [12] X. Wu and S. Fomel, "Automatic fault interpretation with optimal surface voting," *Geophysics*, vol. 83, no. 5, pp. O67–O82, Sep. 2018, doi: [10.1190/geo2018-0115.1](https://doi.org/10.1190/geo2018-0115.1).
- [13] H. Di, M. Shafiq, and G. AlRegib, "Patch-level MLP classification for improved fault detection," in *Proc. SEG Tech. Program Expanded Abstr.*, 2018, pp. 2211–2215, doi: [10.1190/segam2018-2996921.1](https://doi.org/10.1190/segam2018-2996921.1).
- [14] B. Guo, L. Li, and Y. Luo, "A new method for automatic seismic fault detection using convolutional neural network," in *Proc. SEG Tech. Program Expanded Abstr.*, Aug. 2018, pp. 1951–1955, doi: [10.1190/segam2018-2995894.1](https://doi.org/10.1190/segam2018-2995894.1).
- [15] W. Xiong *et al.*, "Seismic fault detection with convolutional neural network," *Geophysics*, vol. 83, no. 5, pp. O97–O103, Sep. 2018, doi: [10.1190/geo2017-0666.1](https://doi.org/10.1190/geo2017-0666.1).
- [16] X. Wu, L. Liang, Y. Shi, and S. Fomel, "FaultSeg3D: Using synthetic data sets to train an end-to-end convolutional neural network for 3D seismic fault segmentation," *Geophysics*, vol. 84, no. 3, pp. IM35–IM45, May 2019, doi: [10.1190/geo2018-0646.1](https://doi.org/10.1190/geo2018-0646.1).
- [17] O. Ronneberger, P. Fischer, and T. Brox, "U-Net: Convolutional networks for biomedical image segmentation," in *Proc. Med. Image Comput. Comput.-Assist. Intervent.*, 2015, pp. 234–241.
- [18] H. Di, C. Li, S. Smith, and A. Abubakar, "Machine learning-assisted seismic interpretation with geologic constraints," in *Proc. SEG Tech. Program Expanded Abstr.*, Aug. 2019, pp. 5360–5364, doi: [10.1190/segam2019-w4-01.1](https://doi.org/10.1190/segam2019-w4-01.1).
- [19] S. Li, C. Yang, H. Sun, and H. Zhang, "Seismic fault detection using an encoder-decoder convolutional neural network with a small training set," *J. Geophys. Eng.*, vol. 16, no. 1, pp. 175–189, Feb. 2019, doi: [10.1093/jge/gxy015](https://doi.org/10.1093/jge/gxy015).
- [20] A. Cunha, A. Pochet, H. Lopes, and M. Gattass, "Seismic fault detection in real data using transfer learning from a convolutional neural network pre-trained with synthetic seismic data," *Comput. Geosci.*, vol. 135, Feb. 2020, Art. no. 104344. [Online]. Available: <https://www.sciencedirect.com/science/article/pii/S0098300418307040>
- [21] Z. Zhou, M. M. R. Siddiquee, N. Tajbakhsh, and J. Liang, "UNet++: Redesigning skip connections to exploit multiscale features in image segmentation," 2019, *arXiv:1912.05074*. [Online]. Available: <http://arxiv.org/abs/1912.05074>
- [22] F. Sultana, A. Sufian, and P. Dutta, "Evolution of image segmentation using deep convolutional neural network: A survey," *Knowl.-Based Syst.*, vols. 201–202, Aug. 2020, Art. no. 106062. [Online]. Available: <https://www.sciencedirect.com/science/article/pii/S0950705120303464>
- [23] H. Huang *et al.*, "UNet 3+: A full-scale connected UNet for medical image segmentation," 2020, *arXiv:2004.08790*. [Online]. Available: <http://arxiv.org/abs/2004.08790>
- [24] X. Qin, Z. Zhang, C. Huang, M. Dehghan, O. R. Zaiane, and M. Jagersand, "U2-Net: Going deeper with nested U-structure for salient object detection," *Pattern Recognit.*, vol. 106, Oct. 2020, Art. no. 107404, doi: [10.1016/j.patcog.2020.107404](https://doi.org/10.1016/j.patcog.2020.107404).
- [25] K. He, X. Zhang, S. Ren, and J. Sun, "Deep residual learning for image recognition," in *Proc. IEEE Conf. Comput. Vis. Pattern Recognit. (CVPR)*, Jun. 2016, pp. 770–778.
- [26] S. M. Mousavi, W. Zhu, Y. Sheng, and G. C. Beroza, "CRED: A deep residual network of convolutional and recurrent units for earthquake signal detection," *Sci. Rep.*, vol. 9, no. 1, Jul. 2019, Art. no. 010267, doi: [10.1038/s41598-019-45748-1](https://doi.org/10.1038/s41598-019-45748-1).
- [27] S. M. Mousavi, W. L. Ellsworth, W. Zhu, L. Y. Chuang, and G. C. Beroza, "Earthquake transformer—An attentive deep-learning model for simultaneous earthquake detection and phase picking," *Nature Commun.*, vol. 11, no. 1, p. 3952, Aug. 2020, doi: [10.1038/s41467-020-17591-w](https://doi.org/10.1038/s41467-020-17591-w).
- [28] J. Watt, R. Borhani, and A. K. Katsaggelos, *Machine Learning Refined: Foundations, Algorithms, and Applications*, 2nd ed. Cambridge, U.K.: Cambridge Univ. Press, 2020.
- [29] S. M. Mousavi and G. C. Beroza, "Bayesian-deep-learning estimation of earthquake location from single-station observations," *IEEE Trans. Geosci. Remote Sens.*, vol. 58, no. 11, pp. 8211–8224, Nov. 2020.
- [30] S. Jadon, "A survey of loss functions for semantic segmentation," in *Proc. IEEE Conf. Comput. Intell. Bioinf. Comput. Biol. (CIBCB)*, Oct. 2020, pp. 1–7.
- [31] C. H. Sudre, W. Li, T. Vercauteren, S. Ourselin, and M. J. Cardoso, "Generalised dice overlap as a deep learning loss function for highly unbalanced segmentations," in *Deep Learning in Medical Image Analysis and Multimodal Learning for Clinical Decision Support*. Cham, Switzerland: Springer, 2017, pp. 240–248.
- [32] A. Paszke *et al.*, "Pytorch: An imperative style, high-performance deep learning library," in *Proc. Adv. Neural Inf. Process. Syst.*, H. Wallach, H. Larochelle, A. Beygelzimer, F. d'Alché-Buc, E. Fox, and R. Garnett, Eds. Red Hook, NY, USA: Curran Associates, 2019, pp. 8024–8035. [Online]. Available: <http://papers.neurips.cc/paper/9015-pytorch-an-imperative-style-high-performance-deep-learning-library.pdf>

- [33] W. Falcon. (2019). *Pytorch Lightning*. [Online]. Available: <https://github.com/PyTorchLightning/pytorch-lightning>
- [34] J. Miller. (2018). *Utah FORGE: 2D and 3D Seismic Data*. [Online]. Available: <https://gdr.openei.org/submissions/1015>
- [35] SEG. (2020). *New Zealand Kerry 3D Data*. [Online]. Available: <https://wiki.seg.org/wiki/Kerry-3D>
- [36] SEG Wiki. (2020). *New Zealand Opunake 3D Data*. [Online]. Available: <https://wiki.seg.org/wiki/Opunake-3D>

**Kai Gao** received the B.Eng. degree in geophysical exploration from the College of Marine Geosciences, Ocean University of China, Qingdao, China, in 2009, and the Ph.D. degree in geophysics from the Department of Geology & Geophysics, Texas A&M University, College Station, TX, USA, in 2014.

He held a post-doctoral position at the Geophysics Group, Los Alamos National Laboratory (LANL), Los Alamos, NM, USA, from 2014 to 2019. He joined the Geophysics Group, LANL, as a Staff Scientist in early 2020, where he is a Staff Scientist. His research focuses on subsurface imaging and inversion, numerical simulation, rock physics, and machine learning for geophysics.

**Lianjie Huang** received the B.Sc. degree in physics and the M.Sc. degree in mathematics from Peking University, Beijing, China, in 1985 and 1989, respectively, and the Ph.D. degree in geophysics from the University of Paris 7/Institut de Physique du Globe de Paris, Paris, France, in 1994.

He is a Senior Scientist with the Geophysics Group, Los Alamos National Laboratory (LANL), Los Alamos, NM, USA. In recent years, he and his team/collaborators use machine learning for seismic imaging and seismic fault detection and characterization. His research areas encompass acoustic and elastic-wave modeling, imaging, and inversion/tomography, with applications to geothermal energy, geologic carbon storage, oil/gas, and cancer detection and characterization.

**Yingcai Zheng** received the B.S. degree in geophysics from Peking University, Beijing, China, in 2001, and the Ph.D. degree in geophysics from the University of California at Santa Cruz, Santa Cruz, CA, USA, in 2007.

He is the Robert and Margaret Sheriff Professor of Applied Geophysics with the Department of Earth and Atmospheric Sciences, University of Houston, Houston, TX, USA. Prior to joining the University of Houston in 2014, he was a Post-Doctoral Fellow and a Research Scientist with the Earth Resources Laboratory, Massachusetts Institute of Technology, Cambridge, MA, USA.

Dr. Zheng was a recipient of the SEG's 2015 Karcher Award for his contribution to exploration geophysics.